A finite element framework for the simulation of bio-inspired adhesives with mushroom-shaped microstructures

M.R. Marulli[a,*], L. Heepe[b], S.N. Gorb[b], M. Paggi[a]

[a] *IMT School for Advanced Studies Lucca, Piazza San Francesco 19, 55100 Lucca, Italy*
[b] *Institute of Zoology, Functional Morphology and Biomechanics, Kiel University, Kiel, Germany*

Abstract

This work proposes a finite element procedure for the simulation of biologically inspired adhesives with a mushroom-shaped patterned surface by formulating a novel interface finite element. The proposed computational method can capture the attachment and detachment mechanisms without modeling in detail the microstructures on the surface, which is the major issue of large-scale simulations involving complex surfaces. A data-driven phenomenological interface constitutive law has been formulated starting from pull-out experimental tests on patterned surfaces with different inclination angles to assess Mode Mixity effects in a range of peeling angles of relevance for applications. The proposed computational model represents a versatile tool for modeling structural problems involving arbitrary shapes components, as in bio-inspired adhesives.

Keywords: Adhesion, bio-inspired surfaces, microstructures, interface finite element, finite rotations.

In memory of Prof. Leon Keer.

1. Introduction

The industrial sector has shown a growing interest in dry adhesives, especially bio-mimetic adhesives inspired by the natural microstructures observed on the animals' skin. The ability of geckos, spiders, and many insects to run up walls and ceilings relies on the unique distribution of microstructures on their feet covered by multiple contact elements [1, 2, 3]. Such natural ways to enhance the biological attachment represent a significant source of information for developing novel artificial bio-inspired adhesives.

The adhesive properties of these natural surfaces are highly influenced by their microstructures geometry. Gecko's footpads are covered by a huge number of keratin hairs, called setae, branching at the tip into hundreds of projections, called spatulae [4]. Next to the more famous microstructures on the gecko's footpads, the attachment systems of beetles from the family Chrysomelidae have inspired the Mushroom-Shaped Adhesive Micro-Structures (MSAMSs) [5]. The beetles' fibrillar surface can be easier reproduced for industrial dry adhesives with better results in comparison with flat surfaces [4]. MSAMSs are usually produced using polymers through soft molding technique. The result is shown in Fig. 1.

The single mushroom-shaped unity that composes the texture of the adhesive, is shown in Fig. 1d. The height of a single pillar is about 100 μm, while the base diameter is 60 μm, decreasing to 35 μm at the middle section and having a neck close to the contact plate with a 25 μm diameter. The contact plate diameter is about 48 μm, and its thickness is 2 μm. The pillar geometry needs to be optimized by considering the stress distribution dependence on the dimension of each part of the pillar to avoid stress singularities [4] that would be critical for the correct adhesion between the substrate and the pillar.

In the case of an optimized geometry, if a tensile load acts on a pillar of the MSAMSs, the pull-off force required for the detachment of the pillar depends upon the tilt angle α (see Fig. 1d).

*Corresponding author
Email address: mariarosaria.marulli@imtlucca.it (M.R. Marulli)

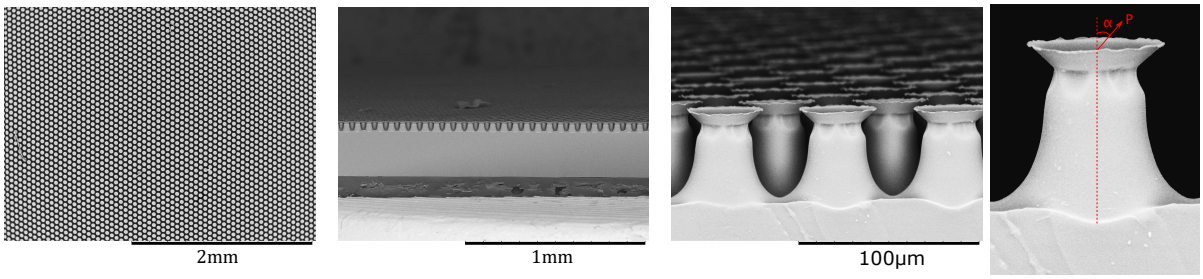

(a) Top view (b) Side view (c) Side view, close up (d) Single pillar

Fig. 1: Mushroom-shaped fibrillar adhesive microstructures made of polyvinylsiloxane (PVS) and detail of a single mushroom-shaped pillar upon the action of a pull-off force P tilted by an angle α.

A detailed review of the experimental and theoretical investigations on the micro-pillars is available in [6]. In the same work, a FE simulation of a single pillar has been used to derive the stress state at the interface between the pillar and the adhering surface. The MSAMSs detachment process has been simulated in [7] testing the frictionless and sticking friction conditions at the contact surface. The adhesive interface of bio-mimetic adhesives has also been simulated through the cohesive zone model in [8, 9] using different traction-separation laws.

Few computational models have been proposed for systems consisting of more than a single pillar due to the computational effort required for meshing the complex geometry of a patterned surface with all its microstructure. An example can be found in [10], regarding a gecko-inspired adhesive pressed against a rigid sphere. Gecko's spatulae have been modeled as a cohesive layer over the tip surface of a seta in [11]. A more complex approach has been proposed in [12] simulating the gecko's microstructure through a 3D multi-scale finite element model. Moreover, the attachment systems of geckos and the adhesive spider web anchorages have been analyzed through the theory of multiple peeling developed in [13] and extended in [14]. This theoretical analysis has been applied in a computational model in [15] to reproduce the contact formed between a smooth substrate and individual tape-like terminal elements. A 'fractal gecko hairs' model composed of multiple layers of self-affine brush structures has been proposed in [16] to simulate the hierarchical fibrillar structure of gecko's footpads and the dependence of the adhesion strength on the direction of pulling. The orientation-dependent adhesion has been further investigated in [17].

Nowadays, it would be desirable to have a suitable computational tool that could be used to scale up the individual pillar's behavior and study complete devices separated by patterned adhesives. For this reason, the present work aims at reproducing the mushroom patterned adhesive performance through the formulation of a phenomenological interface constitutive law that can be incorporated into a zero-thickness interface finite element. In this way, advanced applications of MSAMSs adhesives can be investigated with a reduced computational effort, albeit preserving the accuracy in the adhesive mechanical response.

The starting point of the proposed computational framework is the experimental data acquired during pull-off tests on adhesives' samples, focusing the attention on the dependence of the adhesion strength on the tilt angle, which is a crucial parameter of the performance of the adhesive, see Sec. 2. The interface finite element formulation is then proposed in Sec. 4, and the experimental results allow establishing a data-driven interface constitutive model for the adhesive interface, as proposed in Sec. 3. Finally, Sec. 5 discusses an application example and highlights possible future developments.

2. Experimental investigation

The experimental campaign has been carried on at the University of Kiel by using MSAMSs samples produced with polyvinylsiloxane (PVS) in which the elastic modulus is about 3 MPa. The mushroom-shaped pillars are hexagonally packed on the sample's surface, as shown in Fig. 1a in Sec. 1 and the tests measure the overall behavior of the textured surface.

The adhesion measurements have been performed on a custom-built apparatus, shown in Fig. 2, at a constant velocity of 0.1mm/s, composed by a 6-axes positioning table. The samples have been pressed against a glass cylinder with 5 mm diameter and later retracted from it, considering a defined tilt angle α with respect to the vertical axis of the set-up. Nine tilt angle values have been tested from 0° up to 4° with a step of 0.5°. For each angle, about 30 cycles of attachment (loading) and detachment (unloading) have been considered using decreasing values of the maximum loading displacement ranging between -0.80 mm up to -0.1 mm.

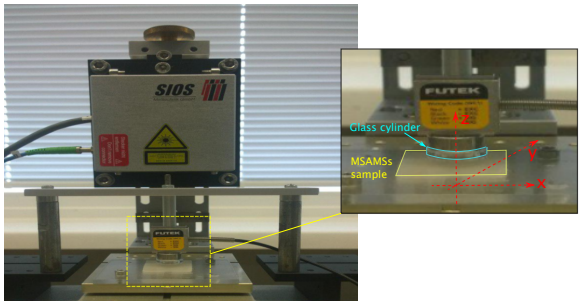

Fig. 2: Experimental set-up for adhesion measurements and magnification with the global reference system.

A typical traction-displacement curve for a single cycle is depicted in Fig. 3, obtained considering the nominal traction T as the ratio between the force value recorded during the experiment and the glass cylinder area. The curves presented in this Section refer to the external global coordinate system of the experimental set-up presented in Fig. 2.. The sign convention adopted in the latter plot and in the rest of the article is consistent with the finite element formulation, assuming loading tractions as negative and adhesive tractions in the unloading phase positive. The detachment stage can be further divided into: (i) an increasing unloading phase up to the maximum traction values corresponding to the pull-off force; and (ii) an unloading decreasing phase till the complete detachment of the adhesive. The division in these two steps is required to identify the maximum adhesive traction and facilitate the data interpolation procedure, as detailed in the next Section. Some relevant quantities are shown in the same plot to introduce the notation: (i) the displacement at the end of the loading phase, g^{u} (afterward referred to as unloading displacement), and the corresponding traction values T^{u}; (ii) the maximum traction T^{ad} and the related displacement g^{ad}; and (iii) the critical displacement at complete adhesive failure, $g^{\max}$.

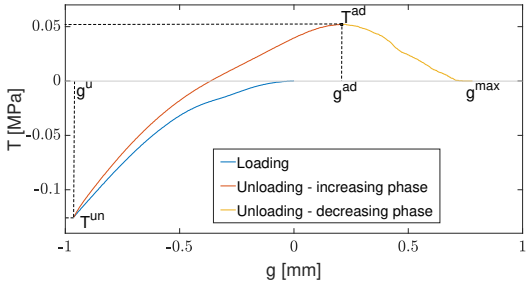

Fig. 3: Experimental curve in terms of imposed displacement g and traction T measured w.r.t. the global reference system in Fig. 2. Tilt angle with respect to the z axis is $\alpha = 2.5°$ and the unloading displacement is $\mathbf{g}^{\mathrm{u}} = -0.81$ mm.

The different cycles related to the same tilt angle have been overlapped in Fig. 4 to observe the effect of the unloading displacement g^{u}.

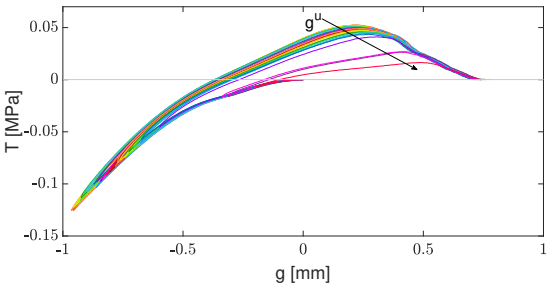

Fig. 4: Experimental curves measured w.r.t. the reference system in Fig. 2 related to the same tilt angle $\alpha = 2.5°$ but with a decreasing unloading displacement g^{u}.

The same procedure has been repeated for each examined tilt angle, and the curves of the first cycle for different tilt angles are shown in Fig. 5. The plot shows that for increasing values of tilt angle, the adhesion peak decreases.

3. Interface Finite Element formulation

The described experimental data are exploited for the formulation of a zero-thickness interface finite element whose kinematics derives from [18]. The numerical framework has been modified by developing a data-driven micromechanics-based interface constitutive law for the analyzed bio-mimetic adhesives. For the sake of brevity, the detailed description of the interface finite element formulation is omitted here. The reader can refer to [18] for

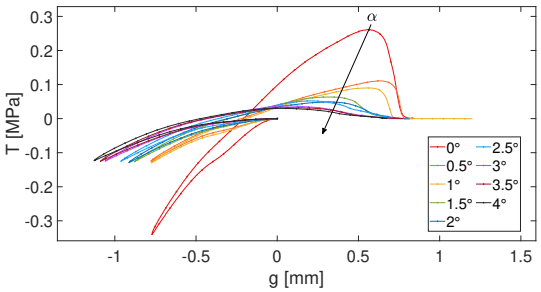

Fig. 5: Experimental traction-displacement curves obtained at the first-cycle, for different tilt angles.

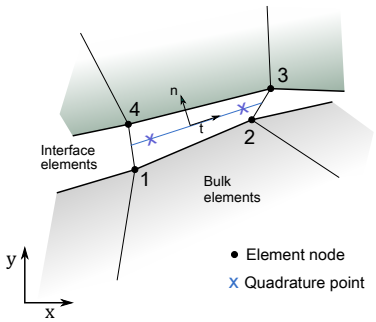

Fig. 6: Sketch of the interface finite element topology.

more details. The hypothesis of small displacement has been put forward.

Focusing the attention on the interface between two solids, referred as Γ, the energy contribution of the interface cohesive traction $\mathbf{T} = (\tau, \sigma)^{\mathrm{T}}$ to the principle of virtual work is given by:

$$\Pi_{\mathbf{int}} = \int_{\Gamma} \mathbf{g}^{\mathrm{T}} \mathbf{T} \mathrm{d}\Gamma \tag{1}$$

where $\mathbf{g} = (g_{\mathrm{t}}, g_{\mathrm{n}})$ describes the gap field across the interface represented by the relative displacement field between the two sides of the interface. The interface finite element topology used for the interface discretization is shown in Fig. 6.

The finite element routine provides the value of the displacement gap $\mathbf{g}$ at each integration point. Hence, the interface model presented in the next Sec, must allow the computation of the cohesive traction $\mathbf{T}$ and the tangent interface constitutive matrix $\mathbb{C} = \dfrac{\partial \mathbf{T}}{\partial \mathbf{g}}$ necessary to solve the nonlinear system of equations deriving from the finite element discretization with a Newton-Raphson scheme.

Let us consider a generic time-step t of a quasi-static finite element analysis. The interface finite element routine provides the tangential and normal components, g_{t} and g_{n}, of the gap vector in the element local reference system. Hence, the local tilt angle $\bar{\alpha}$ can be computed as:

$$\bar{\alpha} = \begin{cases} \arctan\left(\left|\dfrac{g_{\mathrm{t}}}{g_{\mathrm{n}}}\right|\right) & \text{if } g_{\mathrm{n}} \neq 0 \\ 90^{\circ} & \text{if } g_{\mathrm{n}} = 0 \end{cases} \tag{2}$$

The condition and the absolute value are necessary to get $\bar{\alpha} \in [0, 90^{\circ}]$ since the considered experimental angles are assumed to be always positive, and the results are symmetric with respect to the vertical axis. The notation $\bar{\alpha}$ is here introduced to distinguish the tilt angle values referred to the experimental data and the quantities computed during the FE simulation at the element level.

The constitutive model will take the form of $\mathrm{T} = f(g, g^{\mathrm{u}})$ for each experimental tilt angle, hence $\bar{\alpha}$ is compared with the known experimental values, evaluating the interval for which $\bar{\alpha} \in [\alpha_1, \alpha_2]$. In the case of a local tilt angle greater than 4°, the analyzed interval is [4°, 90°] and the traction contribution related to the tilt angle 90° is supposed to be equal to zero. However, the results in this range must be taken with care since they are not based on experimental data.

The modulus of the gap vector is needed as well, and it reads:

$$g = \sqrt{g_{\mathrm{n}}^2 + g_{\mathrm{t}}^2} \tag{3}$$

The interface constitutive law described in the following Section will consider the gap to be negative during the unloading phase, and then it spans from negative to positive values in the unloading phase. For this reason, the gap value used as input in the interface law subroutine must account for the sign as well: the gap g is considered to be negative if $g_{\mathrm{n}} < 0$ and positive if $g_{\mathrm{n}} > 0$.

To obtain the correct traction value for a given gap g, it is essential to identify if the interface is in the loading or unloading phase. In the latter case, it is also necessary to know the unloading displacement g^{u}. For this purpose, two history variables are introduced at each integration point: g_{hist} containing the gap g of the previous timesteps $t-1$, and $g^{\mathrm{u}}_{\mathrm{hist}}$ containing the unloading gap g^{u}. While the variable g_{hist} is updated at each timestep, the variable $g^{\mathrm{u}}_{\mathrm{hist}}$ is updated only during the loading phase such that it remains available for the following unloading phase.

With these inputs, the traction values $\mathrm{T}_1(g, g^{\mathrm{u}})$ for α_1 and $\mathrm{T}_2(g, g^{\mathrm{u}})$ for α_2 are computed selecting the appropriate fitting functions, see Sec. 4. Subsequently, the traction values are linearly interpolated to obtain the traction T and $\frac{\partial \mathrm{T}}{\partial g}$ for the angle $\bar{\alpha}$. The sign of the traction T derives directly from the fitting function.

The final step of the element routine regards the computation of the traction components τ and σ, and the tangent stiffness matrix $\mathbb{C}$. The traction components are evaluated as:

$$\sigma = \mathrm{T}\cos(\bar{\alpha}), \quad \tau = \mathrm{T}\sin(\bar{\alpha}) \tag{4}$$

Since the analytical expression of the interface constitutive law allows the direct computation of the derivative of T with respect to the gap g, after some algebraic manipulation, the tangent constitutive matrix components have been derived as:

$$\mathbb{C}_{1,1} = \frac{\partial \tau}{\partial g_{\mathrm{t}}} = \frac{\partial \mathrm{T}}{\partial g}\frac{g_{\mathrm{t}}}{\sqrt{g_{\mathrm{t}}^2+g_{\mathrm{n}}^2}} + \mathrm{T}\frac{g_{\mathrm{n}}^2}{(g_{\mathrm{t}}^2+g_{\mathrm{n}}^2)^{\frac{3}{2}}} \tag{5a}$$

$$\mathbb{C}_{1,2} = \frac{\partial \tau}{\partial g_{\mathrm{n}}} = \frac{\partial \mathrm{T}}{\partial g}\frac{g_{\mathrm{n}}}{\sqrt{g_{\mathrm{t}}^2+g_{\mathrm{n}}^2}} + \mathrm{T}\frac{-g_{\mathrm{n}}g_{\mathrm{t}}}{(g_{\mathrm{t}}^2+g_{\mathrm{n}}^2)^{\frac{3}{2}}} \tag{5b}$$

$$\mathbb{C}_{2,1} = \frac{\partial \sigma}{\partial g_{\mathrm{t}}} = \frac{\partial \mathrm{T}}{\partial g}\frac{g_{\mathrm{t}}}{\sqrt{g_{\mathrm{t}}^2+g_{\mathrm{n}}^2}} + \mathrm{T}\frac{-g_{\mathrm{n}}g_{\mathrm{t}}}{(g_{\mathrm{t}}^2+g_{\mathrm{n}}^2)^{\frac{3}{2}}} \tag{5c}$$

$$\mathbb{C}_{2,2} = \frac{\partial \sigma}{\partial g_{\mathrm{n}}} = \frac{\partial \mathrm{T}}{\partial g}\frac{g_{\mathrm{n}}}{\sqrt{g_{\mathrm{t}}^2+g_{\mathrm{n}}^2}} + \mathrm{T}\frac{g_{\mathrm{t}}^2}{(g_{\mathrm{t}}^2+g_{\mathrm{n}}^2)^{\frac{3}{2}}} \tag{5d}$$

The algorithm of the presented interface finite element has been condensed in Appendix A.

4. Development of the interface constitutive model

As previously mentioned, the desired constitutive model assumes the form of $\mathrm{T} = f(g, g^{\mathrm{u}})$ for each experimental tilt angle α.

Three different functions have been used to express the fulltraction-separation law: $\mathbf{P}_1(g)$ for the loading phase, $\mathbf{P}_2(g, g^{\mathrm{u}})$ for the increasing unloading phase up to the adhesion peak, and $\mathbf{P}_3(g, g^{\mathrm{u}})$ for the decreasing unloading phase.

Polynomial expressions of the gap have been fitted to the experimental data using the linear least-squares solver with linear constraints offered by Matlab (function *lsqlin*[1] with the default "interior-point" algorithm) which provides the solution to least-squares curve fitting problems of the form:

$$\min_{\mathbf{p}} \quad \frac{1}{2}||\mathbf{C}\cdot\mathbf{p}-\mathbf{T}||_2^2 \qquad \text{s.t.} \begin{cases} \mathbf{A}\cdot\mathbf{p} \le \mathbf{b} \\ \mathbf{A}_{\mathrm{eq}}\cdot\mathbf{p} = \mathbf{b}_{\mathrm{eq}} \end{cases} \tag{6}$$

where $||\ ||_2^2$ indicates the squared Euclidean norm, $\mathbf{p}$ is the vector of the unknown polynomial coefficients, $\mathbf{C}$ collects the displacement data in a matrix form according to the degree of the polynomial, and $\mathbf{T}$ collects the traction values. The inequality and equality constraints are expressed through: (i) the matrices $\mathbf{A}$ and $\mathbf{A}_{\mathrm{eq}}$ containing the powers of the displacement vector; and (ii) $\mathbf{b}$ and $\mathbf{b}_{\mathrm{eq}}$ for the traction values. All these terms are detailed in the following paragraphs.

Collecting the experimental displacement and the traction data of the i-th cycle respectively in the column vectors $\mathbf{g}_i$ and $\mathbf{T}_i$ with $i = 1,..n$ and n number of cycles for the analysed tilt angle, the total displacement vector $\mathbf{g}$ and the total traction vector $\mathbf{T}$ read:

$$\mathbf{g} = \begin{Bmatrix} \mathbf{g}_1 \\ \vdots \\ \mathbf{g}_i \\ \vdots \\ \mathbf{g}_n \end{Bmatrix}, \quad \mathbf{T} = \begin{Bmatrix} \mathbf{T}_1 \\ \vdots \\ \mathbf{T}_i \\ \vdots \\ \mathbf{T}_n \end{Bmatrix} \tag{7}$$

The matrix $\mathbf{C}$ collects hence the element-wise powers of $\mathbf{g}$. As an example, in the case of a third-order polynomial, $\mathbf{C}$ reads:

$$\mathbf{C} = \left[\left\{\mathbf{g}\right\}^3 \left\{\mathbf{g}\right\}^2 \left\{\mathbf{g}\right\} \left\{\mathbf{g}\right\}^0 \right] \tag{8}$$

The matrix $\mathbf{A}$ and $\mathbf{A}_{\mathrm{eq}}$ are used to enforce constraints on the fitting function. The inequality constraint has been used to impose the monotonic increasing (or decreasing) of the function by considering the analytical derivative of the polynomial expression, while the equality condition binds the curve to pass through given couples of traction-gap values. As for the $\mathbf{C}$ matrix, $\mathbf{A}$ and $\mathbf{A}_{\mathrm{eq}}$ collect the powers of the displacement vector, while $\mathbf{b}$ and $\mathbf{b}_{\mathrm{eq}}$ contain the traction vectors. For example, the monotonic decreasing behavior of a third-order polynomial would be expressed as $\mathbf{A}\cdot\mathbf{p} \le \mathbf{b}$ with:

$$\mathbf{A} = \left[3\left\{\mathbf{g}\right\}^2 2\left\{\mathbf{g}\right\} \left\{\mathbf{g}\right\}^0 \left\{\mathbf{0}\right\} \right] \tag{9}$$

[1] See https://it.mathworks.com/help/optim/ug/lsqlin.html

and $\mathbf{b}$ equal to a vector of zero values. The three phases of the experimental curves differ for the polynomial order and the imposed constraints.

It is also necessary to introduce the unloading displacement vector $\mathbf{g}^{\mathrm{u}}$ that collects the unloading displacements of all the cycles, the vector of the unloading traction $\mathbf{T}^{\mathrm{u}}$, and, for the values related to the adhesion peaks, the vectors $\mathbf{g}^{\mathrm{ad}}$ and $\mathbf{T}^{\mathrm{ad}}$.

The loading phase is interpolated using a third-degree polynomial having general expression:

$$\mathbf{P}_1(\mathbf{g}) = p_3\mathbf{g}^3 + p_2\mathbf{g}^2 + p_1\mathbf{g} + p_0 \qquad (10)$$

The vector $\mathbf{p}$ in the minimization problem in Eq. (6) is hence given by $\mathbf{p} = \{p_3, p_2, p_1, p_0\}^{\mathrm{T}}$. Since the polynomial must assume zero value traction at the initial displacement, the fourth coefficient p_0 is always equal to zero. Moreover, the function is constrained to have a monotonic increasing behavior and to pass through the unloading traction-displacement couple of the first cycle since it has been observed that this constraint improves the fitting quality.

The result for $\alpha = 2.5°$ is shown in Fig. 7 where the unloading points for all the cycles are highlighted with red asterisks, and the fitting curve is depicted by the black line. The constraints are satisfied within the default tolerance. The coefficient values found for each α are given in the Appendix A together with all the coefficients that will be computed in the following paragraphs.

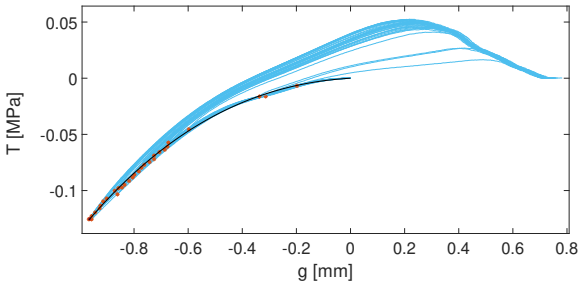

Fig. 7: Loading phase interpolation curve (black line) for $\alpha = 2.5°$. The unloading points for all the cycles are highlighted with red asterisks.

The second step regards the unloading phase. In this case, the fitting procedure of the unloading phase is complicated by the traction's dependency not only on the gap at the interface but also on the unloading displacement g^{u}. The 3D plot in Fig. 8 shows the experimental curves obtained varying g^{u}, which becomes the third axis of the plot. In the same figure, the initial points, the adhesion peaks, and the final points of each curve are highlighted.

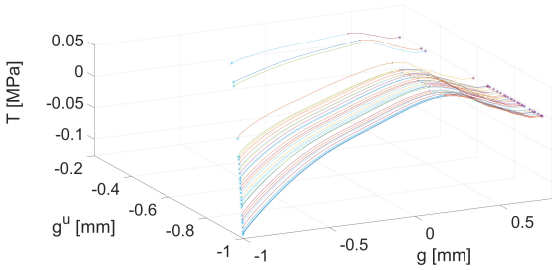

Fig. 8: 3D plot of the unloading phase experimental curves for $\alpha = 2.5°$. For each curve, the initial points, the adhesion peaks and the final points are highlighted.

To improve the convergence of the algorithm used for the minimization problem, the traction values at the adhesive peak $\mathbf{T}^{\mathrm{ad}}$ have been interpolated by a second-order polynomial function of $\mathbf{g}^{\mathrm{u}}$, before being used in the equality conditions. Hence, the fitting function for this case reads:

$$\mathbf{Q}_1(\mathbf{g}^{\mathrm{u}}) = q_2(\mathbf{g}^{\mathrm{u}})^2 + q_1\mathbf{g}^{\mathrm{u}} + q_0 \qquad (11)$$

The polynomial coefficients have been found using Eq. (6) without constraints, and it can be seen in Fig. 9 that the experimental values are very well reproduced by the chosen function.

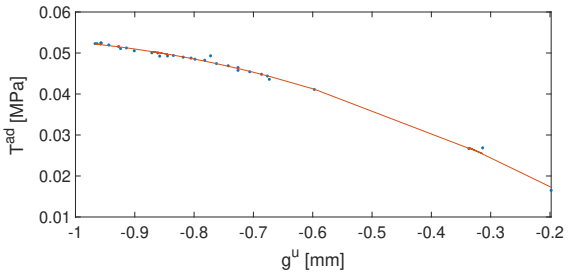

Fig. 9: Fitting of the adhesion peak traction $\mathbf{T}^{\mathrm{ad}}$ with respect to the unloading gap $\mathbf{g}^{\mathrm{u}}$ for $\alpha = 2.5°$.

Going back to the unloading phase fitting procedure, the chosen functions are polynomials of fifth degree in $\mathbf{g}$ and second degree in $\mathbf{g}^{\mathrm{u}}$ having the following general expression:

$$\begin{aligned}\mathbf{P}_i(\mathbf{g}, \mathbf{g}^{\mathrm{u}}) &= p_{00} + p_{10}\mathbf{g} + p_{01}\mathbf{g}^{\mathrm{u}} + p_{20}\mathbf{g}^2 + p_{11}\mathbf{g} \circ \mathbf{g}^{\mathrm{u}} \\ &+ p_{02}(\mathbf{g}^{\mathrm{u}})^2 + p_{30}\mathbf{g}^3 + p_{21}\mathbf{g}^2 \circ \mathbf{g}^{\mathrm{u}} + p_{12}\mathbf{g} \circ (\mathbf{g}^{\mathrm{u}})^2 \\ &+ p_{40}\mathbf{g}^4 + p_{31}\mathbf{g}^3 \circ \mathbf{g}^{\mathrm{u}} + p_{22}\mathbf{g}^2 \circ (\mathbf{g}^{\mathrm{u}})^2 + p_{50}\mathbf{g}^5 \\ &+ p_{41}\mathbf{g}^4 \circ \mathbf{g} + p_{32}\mathbf{g}^3 \circ (\mathbf{g}^{\mathrm{u}})^2\end{aligned} \qquad (12)$$

where ∘ represents the element-wise product.

Equation (6) provides the coefficients vectors for the increasing and the decreasing sections of the unloading phase. The fitting surfaces are shown in Fig. 10 for the branch up to the peak adhesive traction and in Fig. 11 for the post-beak branch.

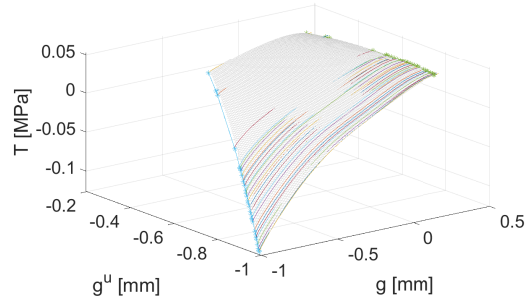

Fig. 10: Experimental curves and fitting surface for the branch up to the peak adhesive tractions of the unloading phase for $\alpha = 2.5°$.

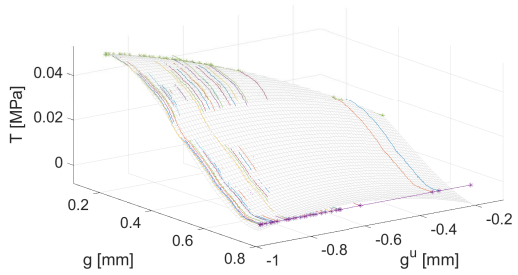

Fig. 11: Experimental curves and fitting surface for the post-peak branch of the unloading phase for $\alpha = 2.5°$.

The fifteen coefficients for the increasing phase have been computed imposing the equality constraints at the unloading points, represented by blue asterisks in Fig. 10, and at the adhesion peaks, shown by green asterisks in the same plot.

For the post-peak branch, the chosen constraints are the equality condition at the adhesive peaks (green asterisks in Fig. 11) and the inequality condition for the fitting surface's monotonic behavior, which must decrease towards zero till the critical displacement (purple asterisks in Fig. 11).

Finally, the complete interface model for a given angle α assumes the form summarised in Tab. 1 and the final result is shown in Fig. 12 for the case of $\alpha = 2.5°$.

The interface routine stores all the polynomial function coefficients and expressions necessary to compute the traction vector according to the gap and to the local tilt angle $\bar{\alpha}$. The interface element subroutine contains the information regarding the experimental critical displacements, $\mathbf{g}^{\mathrm{u}}$, $\mathbf{g}^{\mathrm{ad}}$, and $\mathbf{g}^{\max}$ for each angle α to be compared with the simulation gap g.

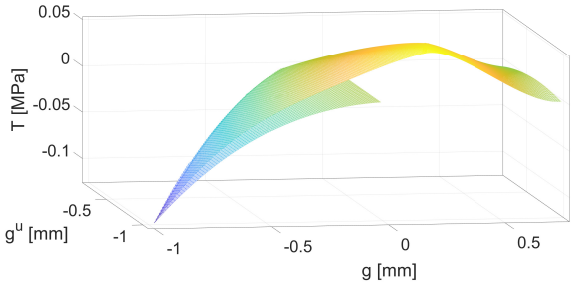

Fig. 12: 3D Fitting surface obtained for $\alpha = 2.5°$.

5. Numerical examples

5.1. *Assessment of the accuracy of the computational model to reproduce the experimental results*

The interface finite element formulation, coded as a new user element in the FE program FEAP version 8.3 [19]. The program employs a full Newton Raphson solution scheme and the simulations converge in at most 3 iterations using the default convergence criteria corresponding to 10^{-16} for the energy norm tolerance and 10^{-8} for the residual norm tolerance.

The interface finite element has been tested using a simple benchmark model to assess the consistency of the numerical implementation and approximation to reproduce the experimental results accurately. The model consists of two square blocks meshed with standard 4-nodes linear finite elements and separated by the interface finite elements (see Fig. 13). The two solids have been considered almost rigid as compared to the interface and with the same material parameters: Young's modulus $E = 1000\,\mathrm{MPa}$ and Poisson ratio $\nu = 0.45$.

The simulation is conducted under displacement control by imposing vertical and horizontal displacements on the upper edge, such that the far-field tilt angle is known. As in the experiments, the simulation considers a loading phase by pressing the upper block against the lower one and then an unloading phase until the interface complete debonding.

Phase	General Form	Intervals	Polynomial order	Number of coefficients
Loading	$\mathbf{T} = P_1(\mathbf{g}, \alpha)$	$\mathbf{g}^{\mathrm{u}} < \mathbf{g} \leq 0$	3^{rd} order in $\mathbf{g}$	4
Unloading - Increasing	$\mathbf{T} = P_2(\mathbf{g}, \mathbf{g}^{\mathrm{u}}, \alpha)$	$\mathbf{g}^{\mathrm{u}} \leq \mathbf{g} < \mathbf{g}^{\mathrm{ad}}$	5^{th} order in $\mathbf{g}$ and 2^{nd} order in $\mathbf{g}^{\mathrm{u}}$	15
Unloading - Decreasing	$\mathbf{T} = P_3(\mathbf{g}, \mathbf{g}^{\mathrm{u}}, \alpha)$	$\mathbf{g}^{\mathrm{ad}} \leq \mathbf{g} \leq \mathbf{g}^{\mathrm{max}}$	5^{th} order in $\mathbf{g}$ and 2^{nd} order in $\mathbf{g}^{\mathrm{u}}$	15

Tab. 1: Summary of the different fitting polynomials used for the interface constitutive model.

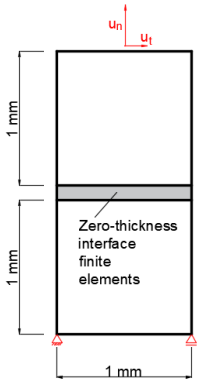

Fig. 13: Benchmark test geometry and boundary conditions with one single interface finite element.

The results for a tilt angle equal to 2.5° are shown in Figs. 14 and compared with the experimental data for different values of $\mathbf{g}^{\mathrm{u}}$. As expected, the model reproduces exactly the fitting functions, and it is in excellent agreement with the experimental data.

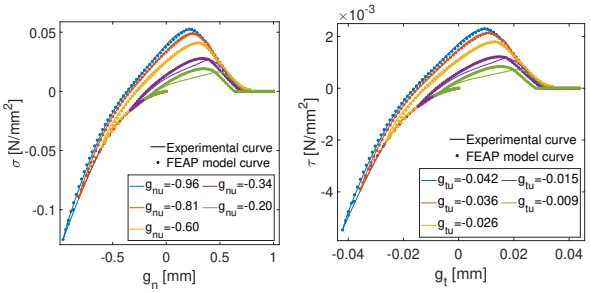

(a) Normal direction. (b) Tangential direction.

Fig. 14: Numerical simulation results compared to experimental and fitting functions for different g^{u} and $\alpha = 2.5°$.

The traction-displacement curves for increasing values of α are shown in Fig. 15 for the normal and the tangential directions. The same unloading displacement has been used for all the simulations. The curves with α equal to $\{\, 0.2°, 0.8°, 1.2° \,\}$ have been obtained through linear interpolation of the known experimental angles, reported in the same plot for comparison. The chosen linear interpolation captures the experimental dependence of the traction on the applied tilt angle with good results.

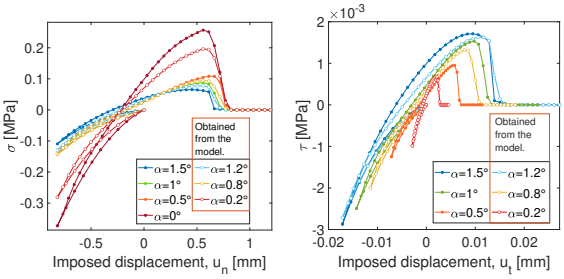

(a) Normal direction. (b) Tangential direction.

Fig. 15: Traction-displacement curves computed by the FE model for different values of α.

5.2. Simulation of a peeling problem.

The proposed computational framework can also model a more realistic application of the MSAMSs adhesive, for example, the simulation of a polymeric layer's bond to a glass substrate through the mushroom-shaped adhesive. The following simulation has been inspired by MSAMSs adhesives usage to realize adhesive gloves for climbing vertical walls. These applications rely on the tilt angle variation to quickly release the gloves from the wall since the detachment force is strictly connected to the peeling angle. Hence, the proposed formulation must correctly capture the force variation with the tilt angle variation over time.

The finite element model used for this simulation is shown in Fig. 16 and consists of a glass substrate layer with Young's Modulus equal to 70 GPa and Poisson ratio equal to 0.3, and an upper polymeric layer in ABS (acrylonitrile butadiene styrene) having $E = 3200$ MPa and $\nu = 0.3$. The interface finite elements have characteristic length $h = 0.17$ mm resulting in 120 elements for the discretization of the interface.

The simulation has been conducted in a quasi-static framework with the far-field angle α depending on the current timestep. After a loading phase with a constant tilt angle $\alpha = 1°$, the interface has been tested, considering firstly an increasing tilt angle and secondly a decreasing one. The results have been compared with those that could be obtained by imposing a constant angle of peeling along the whole interface. The tilt angle evolution has been controlled by checking the local tilt angle at the interface at the last integration point through the Eq. (2), as underlined in Fig. 16a, and it has have been plotted in Fig. 16b. The simulation results in terms of total reaction force per unit width vs imposed displacements are shown in Fig. 16c for the simulations with constant tilt angle (green curve), and for the increasing (blue curve) and decreasing α (red curve) plotted in Fig. 16b.

Figure 17 shows the displacement field magnitude of the joint for the case with constant α at different time-steps: the initial configuration in Fig. 17(a), the end of the loading phase (b) and the unloading steps (c)-(e).

Numerical results show that even a small decrease of α as compared to the uniform tilt angle case, it is sufficient to drop the peeling force and enhance detachment of the mushroom-shaped adhesive.

6. Conclusion

This article presented a novel computational framework for the simulation of bio-inspired adhesives to enhance the simulation of large-scale structural joints that have great potential compared to traditional pressure-sensitive adhesives. In particular, bio-mimetic PVS adhesive samples with mushroom-shaped microstructures have been analyzed in pull-off tests. The team in Lucca has used the experimental data collected by researchers in Kiel to develop a micromechanics-based interface finite element capable of reproducing the adhesive performance as a whole.

The first step regarded the identification of the dominant parameters affecting the adhesive response in the experimental tests. In line with the literature, the MSAMSs adhesive's pull-off strength depended on the maximum load reached during the loading phase and on the tilt angle with which the test is conducted. This last aspect is relevant for the applications since the detachment from the adhering surface can be enhanced by increasing the inclination of the peeling force. The loading and unloading data have been fitted using polynomial surfaces depending on the gap separation between the adhesive surfaces, the unloading gap, and the applied tilt angle. Hence, the functions have been transferred in the interface finite element routine and decomposed in the normal and tangential directions.

After assessing the accuracy of the discretized formulation to reproduce the experimental results, the proposed framework has been exploited to test loading and unloading scenarios involving a polymeric layer bonded onto a glass substrate with a tilt angle variable during the simulation, a situation relevant for MSAMs adhesives that cannot be easily tested in the lab. Results show that small changes of the tilt angle can effectively release adhesion of the adhesive strip. The method's potentiality could be further investigated by extending the method to a 3D setting and simulating more complex applications and prototypes exploiting the patterned adhesives technology.

7. Acknowledgements

The authors would like to thank Dr. Rosaria Del Toro for contributing to the experimental investigation performed with Prof. Gorb's team at the University of Kiel. MP and MRM would like to acknowledge support from MIUR to the project of national interest (PRIN 2017) XFAST-SIMS "Extra fast and accurate simulation of complex structural systems" (GA n. 20173C478N).

References

[1] S. Gorb, Attachment Devices of Insect Cuticle, Springer Netherlands, Dordrecht, 2002.

[2] N. Pugno, E. Lepore, S. Toscano, F. Pugno, Normal Adhesive Force-Displacement Curves of Living Geckos, The Journal of Adhesion 87 (11) (2011) 1059–1072.

[3] Q. Chen, N. M. Pugno, Bio-mimetic mechanisms of natural hierarchical materials: A review, Journal of the Mechanical Behavior of Biomedical Materials 19 (2013) 3–33.

[4] L. Heepe, S. N. Gorb, Biologically inspired mushroom-shaped adhesive microstructures, Annual Review of Materials Research 44 (2014) 173–203.

[5] S. Gorb, M. Varenberg, A. Peressadko, J. Tuma, Biomimetic mushroom-shaped fibrillar adhesive microstructure, Journal of The Royal Society Interface 4 (13) (2007) 271–275.

[6] G. Carbone, E. Pierro, A review of adhesion mechanisms of mushroom-shaped microstructured adhesives, Meccanica 48 (8) (2013) 1819–1833.

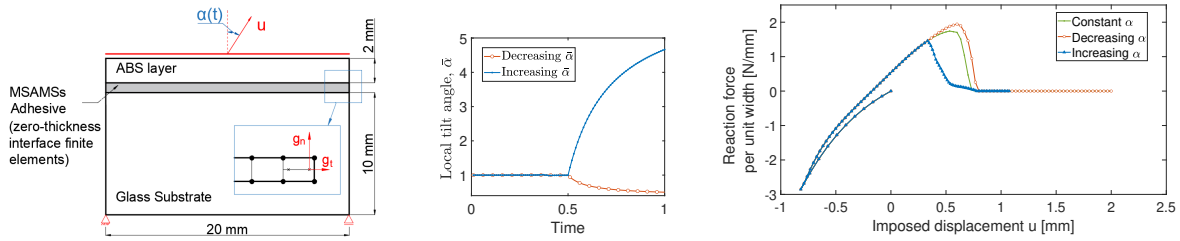

(a) FEM model and detail of the interface last integration point.

(b) Variation of the local tilt angle α.

(c) Force-displacement curves for the peeling test.

Fig. 16: Peeling tests of MSAMSs adhesive bonding an ABS layer to a glass substrate.

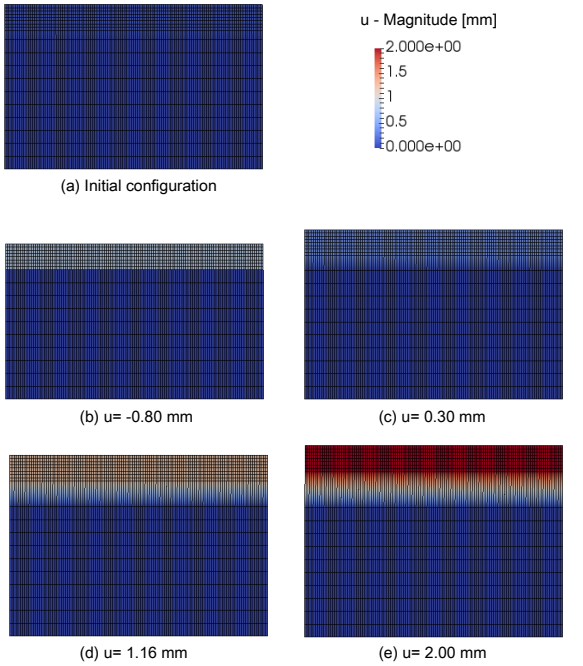

Fig. 17: Snapshots of the simulation with $\alpha = 1°$ showing the magnitude of the displacement field.

[7] A. Spuskanyuk, R. McMeeking, V. Deshpande, E. Arzt, The effect of shape on the adhesion of fibrillar surfaces, Acta Biomaterialia 4 (6) (2008) 1669–1676.

[8] T. Tang, C.-Y. Hui, N. J. Glassmaker, Can a fibrillar interface be stronger and tougher than a non-fibrillar one?, Journal of The Royal Society Interface 2 (5) (2005) 505–516.

[9] X. Zhang, Y. Wang, R. Hensel, E. Arzt, A Design Strategy for Mushroom-Shaped Microfibrils With Optimized Dry Adhesion: Experiments and Finite Element Analyses, Journal of Applied Mechanics 88 (3) (3 2021).

[10] D. Skondras-Giousios, N. E. Karkalos, A. P. Markopoulos, Finite element simulation of friction and adhesion attributed contact of bio-inspired gecko-mimetic PDMS micro-flaps with SiO 2 spherical surface, Bioinspiration & Biomimetics 15 (6) (2020) 066004.

[11] H. Gao, X. Wang, H. Yao, S. Gorb, E. Arzt, Mechanics of hierarchical adhesion structures of geckos, Mechanics of Materials 37 (2-3) (2005) 275–285.

[12] R. A. Sauer, Multiscale modelling and simulation of the deformation and adhesion of a single gecko seta, Computer Methods in Biomechanics and Biomedical Engineering 12 (6) (2009) 627–640.

[13] N. M. Pugno, The theory of multiple peeling, International Journal of Fracture 171 (2) (2011) 185–193.

[14] M. Fraldi, S. Palumbo, A. R. Carotenuto, A. Cutolo, N. M. Pugno, Generalized multiple peeling theory uploading hyperelasticity and pre-stress, Extreme Mechanics Letters 42 (2021) 101085.

[15] L. Brely, F. Bosia, N. M. Pugno, Numerical implementation of multiple peeling theory and its application to spider web anchorages, Interface Focus 5 (1) (2014) 1–9.

[16] H. Yao, H. Gao, Mechanics of robust and releasable adhesion in biology: Bottom-up designed hierarchical structures of gecko, Journal of the Mechanics and Physics of Solids 54 (6) (2006) 1120–1146.

[17] S. Chen, H. Gao, Bio-inspired mechanics of reversible adhesion: Orientation-dependent adhesion strength for non-slipping adhesive contact with transversely isotropic elastic materials, Journal of the Mechanics and Physics of Solids 55 (5) (2007) 1001–1015.

[18] J. Reinoso, M. Paggi, A consistent interface element formulation for geometrical and material nonlinearities, Computational Mechanics 54 (6) (2014) 1569–1581.

[19] O. Zienkiewicz, R. Taylor, J. Z. Zhu, The Finite Element Method: its Basis and Fundamentals: Seventh Edition, Elsevier Ltd, 2013.

Appendix A. Supplementary Material

The list of the fitting function coefficients computed for each tilt angle and the algorithm of the proposed interface finite element can be found in the supplementary material provided together with this article.